

Narrow Fe-K α Reverberation Mapping Unveils the Deactivated Broad-Line Region in a Changing-Look Active Galactic Nucleus

Hirofumi Noda¹, Taisei Mineta¹, Takeo Minezaki², Hiroaki Sameshima², Mitsuru Kokubo³, Taiki Kawamuro⁴, Satoshi Yamada⁴, Takashi Horiuchi², Hironori Matsumoto¹, Makoto Watanabe⁵, Kumiko Morihana⁶, Yoichi Itoh⁷, Koji S. Kawabata⁸, and Yasushi Fukazawa⁹

¹Department of Earth and Space Science, Graduate School of Science, Osaka University, 1-1 Machikaneyama, Toyonaka, Osaka 560-0043, Japan

²Institute of Astronomy, School of Science, the University of Tokyo, 2-21-1 Osawa, Mitaka, Tokyo 181-0015, Japan

³Department of Astrophysical Sciences, Princeton University, Princeton, New Jersey 08544, USA

⁴RIKEN Cluster for Pioneering Research, 2-1 Hirosawa, Wako, Saitama 351-0198, Japan

⁵Department of Physics, Okayama University of Science, 1-1 Ridai-cho, Kita-ku, Okayama, Okayama 700-0005, Japan

⁶Subaru Telescope, National Astronomical Observatory of Japan, 650 North A'ohoku Place, Hilo, HI 96720, USA

⁷Nishi-harima Astronomical Observatory, Center for Astronomy, University of Hyogo, 407-2 Nichigaichi, Sayo-cho, Sayo, Hyogo 679-5313, Japan

⁸Hiroshima Astrophysical Science Center, Hiroshima University, Higashi-Hiroshima, Hiroshima 739-8526, Japan

⁹Department of Physical Science, Hiroshima University, 1-3-1 Kagamiyama, Higashi-Hiroshima, Hiroshima 739-8526, Japan

Abstract

“Changing-look active galactic nuclei” (CLAGNs) are known to change their apparent types between types 1 and 2, usually accompanied by a drastic change in their luminosity on timescales of years. However, it is still unclear whether materials in broad-line regions (BLRs) in CLAGNs appear and disappear during the type-transition or remain at the same location while the line production is simply activated or deactivated. Here we present our X-ray–optical monitoring results of a CLAGN, NGC 3516, by *Suzaku*, *Swift*, and ground telescopes, with our primary focus on the narrow Fe-K α emission line, which is an effective probe of the BLR materials. We detected significant variations of the narrow Fe-K α line on a timescale of tens of days during the type-2 (faint) phase in 2013–2014, and conducted “narrow Fe-K α reverberation mapping,” comparing its flux variation with those of the X-ray continuum from a corona and *B*-band continuum from an accretion disk. We derived, as a result, a time lag of $10.1_{-5.6}^{+5.8}$ days (1σ errors) for the Fe-K α line behind the continuum, which is consistent with the location of the BLR determined in optical spectroscopic reverberation mapping during the type-1 (bright) phase. This finding shows that the BLR materials remained at the same location without emitting optical broad-lines during the type-2 phase. Considering the drastic decrease of the radiation during the type-transition, our result is possibly inconsistent with the hotly-discussed formation models of the BLR which propose that the radiative pressure from an accretion disk should be the main driving force.

Key words: galaxies: active – galaxies: individual (NGC 3516) – galaxies: Seyfert – X-rays: galaxies

1. Introduction

Active Galactic Nuclei (AGNs) are characterized in the optical bands with so-called broad and narrow emission lines with velocity widths of $v_w \gtrsim 1000 \text{ km s}^{-1}$ and several hundreds km s^{-1} , respectively. Whereas the latter are observed in most AGNs, some AGNs almost completely lack the former. Accordingly AGNs are commonly categorized into two types of 1 and 2, depending on whether they show or not, respectively, broad lines (e.g., Seyfert 1943; Khachikian & Weedman 1974). Type-1 AGNs are further categorized into type 1.2, 1.5, 1.8, and 1.9 according to the relative strength of the broad H β to broad H α lines (e.g., Osterbrock 1977; Osterbrock 1981). In types 1.8–1.9, many of the strong opti-

cal broad-lines that are commonly observed in proper type-1 AGNs are absent, and hence their characters are likely to be closer to those in type 2 than type 1. The discovery of hidden broad emission-lines in optical polarized spectra from type-2 AGNs (e.g., Antonucci & Miller 1985; Miller & Goodrich 1990) led to a hypothesis that all AGNs have identical structures consisting of, radially from the center to outer regions, a supermassive black hole (SMBH), X-ray corona, accretion disk, broad-line region (BLR), dusty torus, and narrow-line region (NLR). The hypothesis is now widely accepted and is known as the AGN unified model (Antonucci 1993; Urry & Padovani 1995). In the unified model, the two types are explained in terms of the difference in the viewing angles, where zero degrees is defined in the direction of the polar axis; type-1 AGNs have low viewing angles such that their

BLRs are visible without obscuration by dusty tori, whereas type-2 AGNs have large viewing angles such that their BLRs are obscured by dusty tori.

Although the unified model has been successful in explaining the characteristics of many AGNs for the past three decades, an increasing number of observational results that apparently challenge the unified model have been emerging. One of the most perplexing and thus hotly debated facts is that some AGNs change their types between type 1 and 1.9–2, usually accompanied by luminosity variation by orders of magnitude on a short timescale of several years (e.g., LaMassa *et al.* 2015; MacLeod *et al.* 2016; Ruan *et al.* 2016). The AGNs that have shown this type of event are collectively referred to as “changing-look AGNs (CLAGNs)”. Hereafter, this type of transition phenomenon and its process are referred to as a “changing-look phenomenon” and “changing-look process,” respectively.

The following three hypotheses have been so far proposed to explain the physical mechanisms that cause changing-look phenomena. One explains it in terms of the motion of obscuring clouds into or out of the line of sight, as supported by soft X-ray observations (e.g., Matt *et al.* 2003). One assumes a tidal disruption event (TDE) occurring in an AGN (e.g., Merloni *et al.* 2015). The other proposes that a drastic change in the mass accretion rate causes a drastic change in the luminosity and the spectral energy distribution (SED) of the AGN, which strongly affects BLR materials (e.g., Noda & Done 2018). Since the first one is not caused due to intrinsic changes in the central engine and since the second one seems very rare, we hereafter mainly focus on the third one as the intrinsic changing-look phenomenon.

Noda & Done (2018) studied SED variations through a changing-look process from type-1 (bright) to type-1.9 (faint) states on a typical intrinsic CLAGN, Mrk 1018. They found that the disk black-body emission from a standard disk (Mitsuda *et al.* 1984; Makishima *et al.* 1986) and/or warm Comptonization (soft X-ray excess) emission from a warm disk (e.g., Noda *et al.* 2011; Noda *et al.* 2013) were dominant during the type-1 phase, whereas the hot Comptonization continuum from a hot corona (hot accretion flow; e.g., Yuan & Narayan 2014) was dominant during the type-1.9 phase. In addition, they found that the SED dramatically changed at the transition with an Eddington ratio L/L_{Edd} of a few percent. Since the SED change and the transition point are consistent with those of the high/soft-to-low/hard state transition in Galactic black hole binaries, they suggested that the intrinsic changing-look processes were caused by the state transition between the high/soft and low/hard states of an accretion flow onto a SMBH. Since then, their hypothesis has been verified in other CLAGNs (e.g., Ruan *et al.* 2019; Graham *et al.* 2020). However, it is still unclear how the mass-accretion rate changes drastically in such a short period, which is orders of magnitude shorter than the viscous timescale of the standard disk. The necessity of further studies of the disk structure and the disk instability in the vicinity of a SMBH has been recognized among astronomers in the field.

Another critical question on intrinsic CLAGNs is what happens in BLR materials before and after the drastic luminosity and SED variations of the emission from the accretion flow onto a SMBH. Given that optical broad emission-lines appear or disappear before/after a changing-look process, one possible and perhaps most intuitive scenario is that BLR materials appear in the type-1 phase and disappear in the type-2 phase. Alternatively, it is also possible that the BLR materials remain at the same location in either state and are activated enough to produce optical broad lines in the type-1 phase, whereas they are deactivated not to emit optical broad-lines anymore in the type-2 phase. Conventional optical spectroscopic observations are unsuitable for distinguishing these two scenarios because AGNs do not emit optical broad lines during the type-2 phase by definition. Therefore, another approach is required to address the question.

In order to constrain what happens in BLR materials through the changing-look process, we here study emission in the X-ray band, especially a narrow Fe-K α emission line at 6.4 keV, from a CLAGN. An Fe-K α line is generated through photo-absorption to a hard X-ray continuum originating from a corona near a SMBH caused by materials in the accretion disk, BLR, dusty torus and/or distant molecular disk/clouds. Note that we use the term “narrow Fe-K α line” to mean a non-relativistic iron line with a velocity width from zero to several thousands km s $^{-1}$, which encompasses the velocity widths of both broad and narrow emission lines in the optical band (see §4.1.2).

As the target CLAGN, we select NGC 3516, which used to be recognized as a bright and typical type-1 Seyfert with strong broad emission lines but around 2014 got into the faint type-1.9 or -2 phase, at which the broad lines almost disappeared (Shapovalova *et al.* 2019). Mehdipour *et al.* (2022) analyzed the X-ray data of NGC 3516 derived during the faint phase at 2017, and concluded that the changing-look process can be explained by the change of the ionizing SED without requiring any new or variable obscuration. Therefore, NGC 3516 is an intrinsic CLAGN. In 2020, it returned to the type-1 phase, where optical broad lines reappeared (Oknyansky *et al.* 2021). We performed X-ray and optical simultaneous monitoring observations between 2013 and 2014, during which NGC 3516 was almost in the type-2 phase, with the X-ray astronomical satellite *Suzaku* and optical 1.5-m class ground telescopes in Japan (Noda *et al.* 2016). In the present study, we investigate the variability of the narrow Fe-K α emission line at 6.4 keV on the timescale of a week to a year which corresponds to radii from a BLR to a dusty torus, and conduct the “narrow Fe-K α reverberation mapping” by comparing it with the X-ray and optical continuum variabilities.

The present paper is organized as follows. Observations and data reductions are summarized in section 2 (n.b., part of the data were described in Noda *et al.* 2016). Spectral analyses of the X-ray continuum and narrow Fe-K α line, light-curves and timing analyses, including cross-correlation and JAVELIN analyses, are described in section 3. Finally, we discuss what happens in the BLR materials before and after

Table 1. X-ray observations in the faint phase of NGC 3516 by *Suzaku*.

Epoch	ObsID	Observation Start (UT)	Observation End (UT)	Middle (MJD)	Exposure (ksec)
1	708006010	2013-04-09T23:13:20	2013-04-11T01:06:16	56392.5	51.40
2	708006020	2013-04-27T00:17:13	2013-04-27T10:42:22	56409.2	19.12
3	708006030	2013-05-12T00:22:24	2013-05-13T02:30:23	56424.6	50.43
4	708006070	2013-05-23T03:32:08	2013-05-24T07:05:07	56435.7	51.48
5	708006040	2013-05-29T11:02:50	2013-05-30T15:15:14	56442.0	54.22
6	708006060	2013-11-04T06:15:13	2013-11-05T05:10:17	56600.7	46.20
7	708006080	2014-04-07T16:54:26	2014-04-08T12:00:24	56755.1	51.54
8	710009010	2015-05-12T08:01:41	2015-05-15T00:50:12	57155.7	117.7

transitions and derive constraints to the BLR origin in section 4, comparing our results with previous multi-wavelength studies and those of the narrow Fe-K α line. We adopt cosmological parameters of $H_0 = 73 \text{ km s}^{-1} \text{ Mpc}^{-1}$, $\Omega_\Lambda = 0.73$ and $\Omega_m = 0.27$ throughout the present paper. Errors quoted in this paper refer to 1σ errors unless noted otherwise.

2. Observations and Data Reduction

We performed X-ray and optical simultaneous monitoring of the CLAGN NGC 3516 from 2013 April to 2014 April, during which NGC 3516 was in the type-2 (faint) phase (PI: H. Noda). The X-ray observations were performed on seven occasions with the X-ray astronomical satellite *Suzaku*. The first five (Epochs 1–5) were conducted with intervals of 1–2 weeks, and the last two (Epochs 6–7) were with intervals of about half a year, all with exposures of ~ 50 ksec except for the second observation with ~ 19 ksec. The details of the observations are same as those of Noda et al. (2016), and presented in Table 1. The data of the X-ray Imaging Spectrometer (XIS; Koyama et al. 2007) were obtained with its normal mode and processed with the software version 2.4. The front-illuminated XIS0 and 3 data were merged and used for our analyses, whereas the back-illuminated XIS1 data were not used because the background around 6 keV was high. We extracted source events from a circular region with a radius of $180''$ and background events from an annular region with inner and outer radii of $270''$ and $360''$, respectively. The response and ancillary-response file were produced with the software packages *xisrmfgen* and *xissimarfgen* (Ishisaki et al. 2007), respectively, in HEASOFT-6.28. In the present paper, we did not use the data of the Hard X-ray Detector (HXD; Takahashi et al. 2007).

In addition to the data of the densely-sampled seven *Suzaku* observations, we used more X-ray data as follows. We observed NGC 3516 with *Suzaku* one more time on 2015 May 12 (Epoch 8) with an exposure time of ~ 118 ksec as shown in Table 1. We reduced the data in the same way as the previous seven *Suzaku* datasets and combined them in our X-ray analyses. Furthermore, the Neil Gehrels *Swift* Observatory (hereafter, *Swift*) monitored NGC 3516 in 2012–2013 and 2014–2015, the timings of which were shortly before and after our intensive X-ray–optical simultaneous monitoring in

2013–2014, respectively. We used the data of the *Swift* X-Ray Telescope (XRT) with the Photon Counting (PC) mode in X-ray analyses together with *Suzaku*/XIS. The number of the XRT datasets with the PC mode is 56. We reduced the XRT data with the automated pipeline provided by the UK *Swift* Science Data Centre (Evans et al. 2007; Evans et al. 2009) and obtained X-ray spectra. In the present paper, we did not use the Ultraviolet/Optical Telescope (UVOT) and Burst Alert Telescope (BAT) data of the *Swift* observations.

Optical observations of NGC 3516 were performed in the *B* band with four ground-based telescopes in Japan, Pirka, Kiso Schmidt, Nayuta, and Kanata. The *Suzaku* observations in Epochs 1–7 were simultaneously covered, and in addition, the intervals between them were also densely covered, typically once per day. The image data were reduced in the standard manner for CCD detectors with IRAF. We derived the *B*-band flux of NGC 3516 in every image with differential image photometry, in which we subtracted a reference image from every image by matching the point-spread function profile and performed aperture photometry using reference stars. We successfully derived a *B*-band variable component after subtracting a stable component including the host galaxy emission. The detail of the method is described in Noda et al. (2016). The flux-density data of the *B*-band light curve derived with the differential image photometry were published in Noda et al. (2016). In the present analyses, we used flux density values with an artificial 0.5 mJy offset in order to circumvent negative flux densities, which happened, depending on the choice of the reference image (see Fig. 4 in Noda et al. 2016). The offset does not affect the timing analyses in §3.

3. Data Analyses and Results

3.1. X-ray, optical, and narrow Fe-K α light curves

Figure 1 showed the extracted 2–10 keV spectra from the *Suzaku* data. The spectra in Epochs 1–7 are practically the same as those in Figure 3 in Noda et al. (2016) because the datasets are same, whereas the spectrum in Epoch 8 (orange in Figure 1) was newly added in this study. We fitted them individually with a model of a photo-absorbed power-law function and two Gaussians, or `phabs*zashift*(cflux*powerlaw + cflux*gaussian + cflux*gaussian)` in the XSPEC

Table 2. Results of the spectral fits to the eight *Suzaku* datasets of NGC 3516.

	MJD	56392.5	56409.2	56424.6	56435.7	56442.0	56600.7	56755.1	57155.7
Model	Parameter	Epoch 1	Epoch 2	Epoch 3	Epoch 4	Epoch 5	Epoch 6	Epoch 7	Epoch 8
phabs	N_{H}^a	$1.35^{+0.23}_{-0.22}$	1.49 ± 0.18	0.91 ± 0.09	1.03 ± 0.08	0.93 ± 0.10	$1.31^{+0.29}_{-0.28}$	$2.93^{+0.40}_{-0.39}$	1.57 ± 0.07
zashift	z	0.00884 (fix)							
powerlaw	Γ	1.34 ± 0.06	1.61 ± 0.05	1.63 ± 0.03	1.75 ± 0.02	1.62 ± 0.03	1.45 ± 0.08	$1.49^{+0.11}_{-0.10}$	1.60 ± 0.02
	F_{2-10}^b	0.44 ± 0.01	1.52 ± 0.02	2.14 ± 0.02	2.68 ± 0.02	1.60 ± 0.01	0.31 ± 0.01	0.21 ± 0.01	1.64 ± 0.01
gaussian1	E	6.4 keV (fix)							
	$F_{6.4}^c$	2.37 ± 0.15	2.03 ± 0.32	$3.18^{+0.24}_{-0.23}$	3.47 ± 0.25	3.42 ± 0.21	1.8 ± 0.14	1.57 ± 0.12	2.78 ± 0.15
	$\text{EW}_{6.4}^d$	$459.5^{+34.7}_{-27.1}$	$120.5^{+20.6}_{-19.6}$	$134.9^{+10.3}_{-9.4}$	$121.5^{+9.4}_{-8.6}$	$192.8^{+12.3}_{-11.6}$	$506.2^{+50.1}_{-36.5}$	$667.9^{+70.6}_{-46.9}$	$151.6^{+8.8}_{-8.1}$
gaussian2	E	6.97 keV (fix)							
	$F_{6.97}^e$	4.8 ± 1.2	4.4 ± 3.1	< 4.1	3.5 ± 2.4	3.3 ± 1.9	1.9 ± 1.0	4.2 ± 1.0	3.0 ± 1.4
	$\text{EW}_{6.97}^f$	$95.6^{+26.1}_{-21.9}$	$27.9^{+19.8}_{-18.6}$	< 18.2	$13.0^{+8.5}_{-8.4}$	$19.8^{+11.4}_{-10.4}$	$56.2^{+31.7}_{-30.2}$	$188.9^{+55.3}_{-43.0}$	$17.4^{+8.5}_{-8.1}$
	L_{2-10}^g	0.72 ± 0.02	2.33 ± 0.07	3.43 ± 0.03	4.23 ± 0.03	2.58 ± 0.02	0.51 ± 0.02	0.32 ± 0.02	2.52 ± 0.02
$\chi^2 / \text{d.o.f.}$		456.2/517	552.5/598	1446.5/1503	1570.7/1579	1434.5/1393	339.6/356	210.9/261	1884.0/1731

^aEquivalent hydrogen column density in 10^{22} cm^{-2} .

^bUnabsorbed 2–10 keV flux of the powerlaw component in $10^{-11} \text{ erg s}^{-1} \text{ cm}^{-2}$.

^cUnabsorbed flux of gaussian1 at 6.4 keV in $10^{-13} \text{ erg s}^{-1} \text{ cm}^{-2}$.

^dEquivalent width of gaussian1 at 6.4 keV in eV.

^eUnabsorbed flux of gaussian2 at 6.97 keV in $10^{-14} \text{ erg s}^{-1} \text{ cm}^{-2}$.

^fEquivalent width of gaussian2 at 6.97 keV in eV.

^gThe 2–10 keV luminosity in $10^{42} \text{ erg s}^{-1}$.

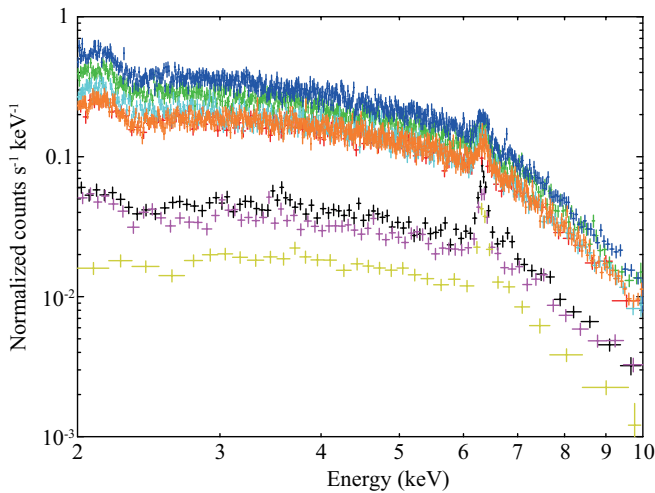


Figure 1. X-ray spectra of NGC 3516 obtained in the eight *Suzaku* observations in black, red, green, blue, cyan, magenta, yellow, and orange for Epochs 1 to 8, respectively.

notation. For convenience, we hereafter express the first and second gaussian models as `gaussian1` and `gaussian2`, respectively. Here, the power-law model reproduces an X-ray continuum from a corona, `gaussian1` models a narrow and neutral Fe-K α emission line at 6.4 keV, and `gaussian2` models a narrow hydrogen-like Fe emission-line at 6.97 keV. The use of `gaussian1` is mainly different from the model employed in Noda *et al.* (2016), where they used the `pexmon` model (Nandra *et al.* 2007). The `pexmon` model includes a reflection continuum in addition to the narrow Fe-K α line as in `gaussian1`. However, the `pexmon` flux was determined almost solely by the narrow Fe-K α line because the reflection component is much weaker than the power-law continuum in this band, 2–10 keV. Hence, we adopted `gaussian1` in this study for simplicity, given that the difference of the models would make no significant difference in the results. In the fitted model, we considered the redshift (z) by convolving `zashift` with z fixed at 0.00884. We convolved the `cflux` models to the individual components to measure their fluxes. In the

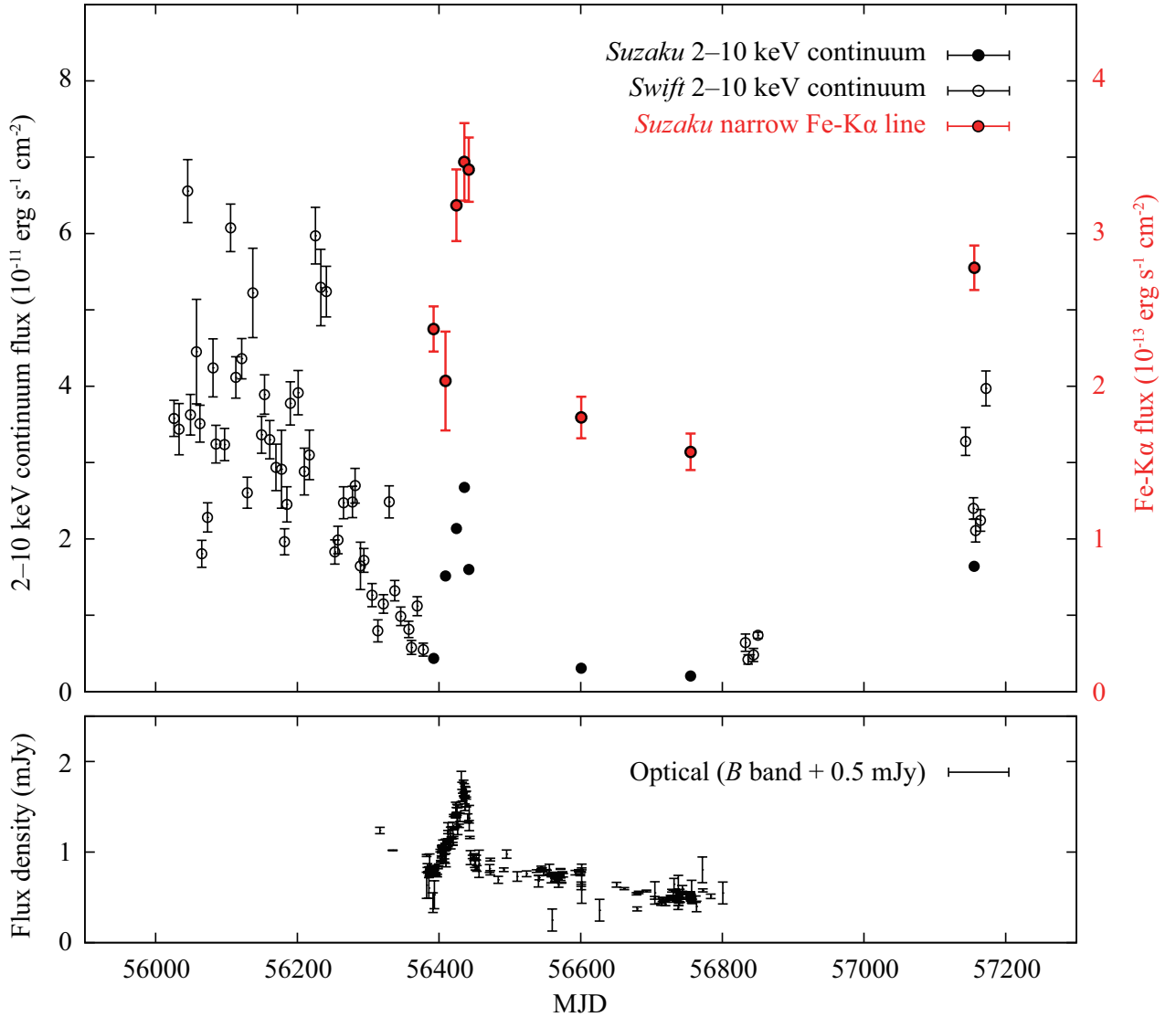


Figure 2. (Top) 2–10 keV continuum flux in black and narrow Fe-K α emission line flux in red. Filled and open circles are the data of *Suzaku* (Table 2) and *Swift*, respectively. (bottom) *B*-band light curve with an 0.5 mJy offset.

spectral fitting, the column density (N_{H}) of `phabs` and the photon index (Γ) of `powerlaw` were allowed to vary. The energies of the two `gaussian` components were fixed at 6.4 keV and 6.97 keV, and so were their sigmas at 0 eV. The fluxes of all the `cflux` models were allowed to vary, and their minimum and maximum energies between which the fluxes were calculated were fixed at 2 and 10 keV, respectively. Spectral fitting was based on the χ^2 statistics. As a result, all the fits were broadly successful with reduced $\chi^2 < 1.09$. Table 2 tabulates the fitting result for all the eight *Suzaku* observations of NGC 3516.

To check the presence of a broader component around 6.4 keV, we added one more gaussian model with the energy fixed at 6.4 keV, and the sigma and normalization left free. To also check the energy shift of `gaussian1`, we allowed its energy to vary, and fitted all the *Suzaku* spectra. As a result, a broad component with the sigma consistent with 700 eV within 1σ errors was not ruled out in all the

epochs except for Epoch 7 in which the source was too faint to constrain the broad component. The energy and flux of `gaussian1`, and the 2–10 keV flux of `powerlaw` became consistent within 1σ errors with those in the fits without the broad component (Table 2). Therefore, the analyses from §3.2 on were not affected by ignoring the presence of the broad component. As modeled by `pexmon` in Noda et al. (2016), most of the broad component is considered to be a part of a non-relativistic reflection continuum with the Fe-K absorption edge at 7.1 keV because it is accompanied by the narrow Fe-K α line, although a relativistically-blurred reflection and/or a partially-absorbed power-law continuum might be included. We also fitted all the *Suzaku* spectra allowing the energy of `gaussian2` to vary, and confirmed that it can be located in a range of 6.7–7.2 keV considering 1σ errors. This range includes energies of not only hydrogen-like Fe but also helium-like Fe and Fe-K β emission lines. Whereas the Fe-K β line is associated with the Fe-K α line at 6.4 keV,

the hydrogen- and helium-like Fe lines must be emitted in a highly ionized region, which might be a radiatively inefficient accretion flow as reported in low-luminosity AGNs (e.g., Dewangan *et al.* 2004). The detailed interpretations of the broad component and the highly-ionized emission lines are beyond the scope of this paper, they will be discussed in subsequent papers.

We analyzed the *Swift* data as follows. We first made an averaged spectrum in 2–10 keV from 56 datasets and fitted it with a model of `phabs*zashift*(cflux*powerlaw + cflux*gaussian1)` with χ^2 statistics. Here, we did not include `gaussian2` in the model, unlike our analysis of the *Suzaku* data, because of low statistics in the *Swift* spectra at energies around ~ 6.97 keV. The energy and sigma of `gaussian1` were fixed at 6.4 keV and 0 eV, respectively. The parameters N_{H} of `phabs`, Γ and flux of `powerlaw`, and the flux of `gaussian1` were allowed to vary. The redshift in `zashift` was fixed at $z = 0.00884$. The resultant fit was successful with $\chi^2/\text{d.o.f.} = 295.14/289$. The best-fit `gaussian1` flux was $(3.78 \pm 1.02) \times 10^{-12} \text{ erg s}^{-1} \text{ cm}^{-2}$ (1σ error). Even in the averaged spectral fit merging 56 data, the uncertainty of the narrow Fe-K α flux is larger than that of a *Suzaku* single epoch by a factor of $\gtrsim 4$ because of low sensitivity. Hence, in the following analysis, we did not use the *Swift* data to constrain the narrow Fe-K α flux. Then, we extracted a 2–7 keV spectrum from every *Swift* data, totaling 56 spectra, and fitted the individual spectra with basically the same model but with the C-statistics. Here, we ignored the 7–10 keV band in individual spectra because counts at energies above 7 keV are too low. In the fitting, we fixed N_{H} of `phabs` and Γ of `powerlaw` at the values obtained in the averaged-spectral fit. Again, the narrow Fe-K α fluxes could not be constrained in the individual *Swift* spectra because of too low statistics. As a result, all the fits were acceptable, and we determined the 2–10 keV fluxes from the individual *Swift* spectra.

Figure 2 shows the 2–10 keV continuum light-curves for ~ 1200 days obtained from the *Suzaku* and *Swift* spectral analyses. The 2–10 keV continuum flux almost monotonously decreased from MJD 56000 to 56390 and got into the faint phase. Then, it showed a significant flare by an order of magnitude from MJD 56393 to 56440 peaking at MJD 56436, and returned into the faint phase. The faint phase continued until MJD 56800, and it re-brightened around MJD 57200. Figure 2 also shows the *B*-band light curve, which has similar variation to the 2–10 keV light curve. As already reported by Noda *et al.* (2016), the 2–10 keV continuum and the *B*-band light curves showed a strong positive correlation with a high cross-correlation coefficient of > 0.95 . Noda *et al.* (2016) performed the Interpolation Cross Correlation Function (ICCF) and JAVELIN analyses (see §3.2 for details of the methods) and determined the *B*-band time lag behind the X-ray continuum to be $2.0^{+0.7}_{-0.6}$ days (1σ errors).

Figure 2 also shows the narrow Fe-K α line light curve. The narrow Fe-K α flux also showed an apparent flare during MJD 56409–56442 with its peak likely follow those of the

2–10 keV and *B*-band light curves. After the flare, it became faint until MJD 56755 and re-brightened at MJD 57156, similarly to the 2–10 keV light curve. We fitted the narrow Fe-K α light curve from MJD 56393 to 57156 (Epochs 1–8) with a constant model and found that the model was rejected with $\chi^2/\text{d.o.f.} = 111/6$, proving that the observed time-variations are significant. Fitting only five points in the peak at MJD 56393–56442 (Epochs 1–5) with a constant model resulted in $\chi^2/\text{d.o.f.} = 15.1/3$, confirming the variability. Therefore, we conclude that the narrow Fe-K α flux of NGC 3516 showed a significant variation on a timescale within ~ 50 days in MJD 56393–56442.

Table 2 shows that the equivalent width (EW) of the narrow Fe-K α line reached ~ 670 eV (Epoch 7), which is larger by a factor of ~ 7 than those in typical type-1 AGNs (e.g., Ricci *et al.* 2013). The main reason for the large EW appears to be not an intrinsic increase of the line flux but a decrease of the continuum flux; while the 2–10 keV continuum flux decreased by a factor of ~ 13 , the narrow Fe-K α flux varied only by a factor of ~ 2 . This indicates that the narrow Fe-K α flux consists of a variable component that varied on timescales of a week to months and a stationary component that remained stable for a year (Epochs 1–7). Here, we can regard the lowest Fe-K α flux of $\sim 1.6 \times 10^{-13} \text{ erg s}^{-1} \text{ cm}^{-2}$ at Epoch 7 as the upper limit of the stationary flux during our observation period, because the variable 2–10 keV continuum flux was minimum in the epoch. We discuss the variable and stationary fluxes furthermore in §3.4.

3.2. ICCF analyses

Using the high-quality long-term 2–10 keV continuum, *B*-band, and narrow Fe-K α light curves, we determine the amount of the time lag (τ) of the narrow Fe-K α flux variation to the X-ray and/or optical continuum variations. We started from the standard cross-correlation analysis called ICCF (Peterson *et al.* 1998) in this subsection, which has been employed in many AGN reverberation studies, before employing the more complex JAVELIN method in the next subsection. The ICCF method interpolates neighboring two data points with a linear function and conducts the traditional cross-correlation analysis. The method can be applied to two light curves regardless of whether they were simultaneously sampled or not. In the present paper, we employed the PYCCF algorithm¹.

We first applied the ICCF analysis to a pair of the 2–10 keV continuum and narrow Fe-K α light curves (Figure 2 (top)) and estimated their time lag τ . The range of τ was set from -300 to 300 days. The number of iterations was 10000. The threshold of the r value to judge correlations significant was set to 0.4, which corresponds to the 99% significance level with $\text{d.o.f.} = 40$. In error estimation, we employed the Flux Randomization (FR) and Random Subset Selection (RSS). Figure 3 left-panels show the derived cross-correlation functions (CCF) and the distribution of the CCF centroid (CCCD) of τ . The time lag τ was determined to be $8.0^{+12.6}_{-33.2}$ days

¹ We employed the code `pyCCF` in <http://ascl.net/code/v/1868>

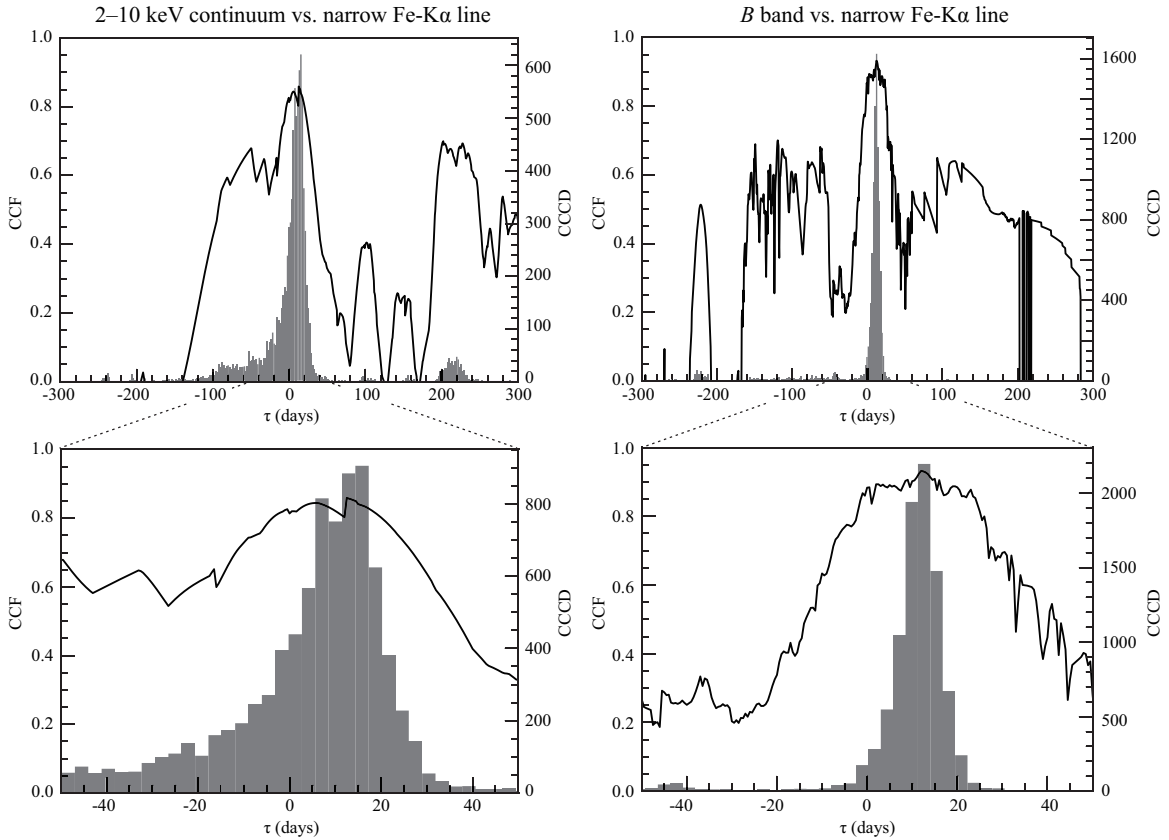


Figure 3. Left panels show the results of ICCF analyses of the NGC 3516 data for the time lag τ of -300 to 300 days between the 2–10 keV continuum and the narrow $\text{Fe-K}\alpha$ light curves. A positive value of τ indicates that 2–10 keV continuum flux precedes the corresponding narrow $\text{Fe-K}\alpha$ flux. Right panels show those with the B -band and narrow $\text{Fe-K}\alpha$ light curves. Bottom panels show zoomed-up histograms for a range of -50 to 50 days in the top panels. Black solid lines show cross-correlation functions (CCFs), and gray histograms show the distribution of the CCF centroids (CCCDs).

(1σ errors). The error on the negative side is much larger than that on the positive side because both 2–10 keV continuum and narrow $\text{Fe-K}\alpha$ data were sparse after their peaks at MJD 56393–56442.

We next applied the same ICCF analysis in the calculation settings to the B -band light curve (Figure 2 bottom) and narrow $\text{Fe-K}\alpha$ light curve. Figure 3 right-panels show the derived CCF and CCCD of τ . The result is consistent, within errors, with the ICCF analysis with the 2–10 keV continuum and τ was more tightly constrained to be $10.9^{+4.5}_{-9.4}$ days (1σ errors), owing to the denser data points of the B -band light curve than those of the 2–10 keV continuum, in particular after the flare peak at MJD 56393–56442. The B -band flux was already confirmed to show a strong correlation with the X-ray continuum flux with a small time lag of ~ 2 days (Noda et al. 2016). Hence, we consider that the obtained τ between the B -band and narrow $\text{Fe-K}\alpha$ gives a good indication for τ between the X-ray continuum and narrow $\text{Fe-K}\alpha$. Table 3 summarizes the obtained time lags τ .

3.3. JAVELIN analyses

In this subsection, we introduce a transfer function which reflects the source geometry of the narrow $\text{Fe-K}\alpha$ emission line. For this purpose, we conducted the JAVELIN analysis (Zu et al. 2011; Zu et al. 2013). In the JAVELIN process, the

continuum variability is assumed to follow a damped random walk function, and a simple top-hat shape transfer function is convolved to reproduce the line variability. The damped random walk function is described in terms of the Gauss process with a kernel which includes parameters of amplitude and the time constant. The top-hat transfer function has three parameters, the time lag τ , width w , and scale A . The JAVELIN process fits the continuum and line light curves, searching for the best-fit parameters through the Markov chain Monte Carlo (MCMC) method.

We performed the JAVELIN analysis using the 2–10 keV continuum and narrow $\text{Fe-K}\alpha$ light curves as the primary and reprocessed components, respectively. First, we used the entire period of the 2–10 keV light curve. Considering the time lag obtained with the ICCF analyses (Figure 3) and its uncertainties, we set a flat prior distribution of τ from -50 to 50 days. If $w/2$ is larger than τ , the transfer function violates causality. Hence, we assumed the flat prior distribution of w to fall within a range of 0 to 30 days, which is not much larger than the time lag. We also assumed a flat prior distribution of A to be from 0 to 0.10 to suppress the possibility of unrealistically large amplitudes of the narrow $\text{Fe-K}\alpha$ variation during periods in which no data points are present. Note that $A = 0.10$ corresponds to an amplitude of ~ 16 times larger than the observed one from MJD 56393

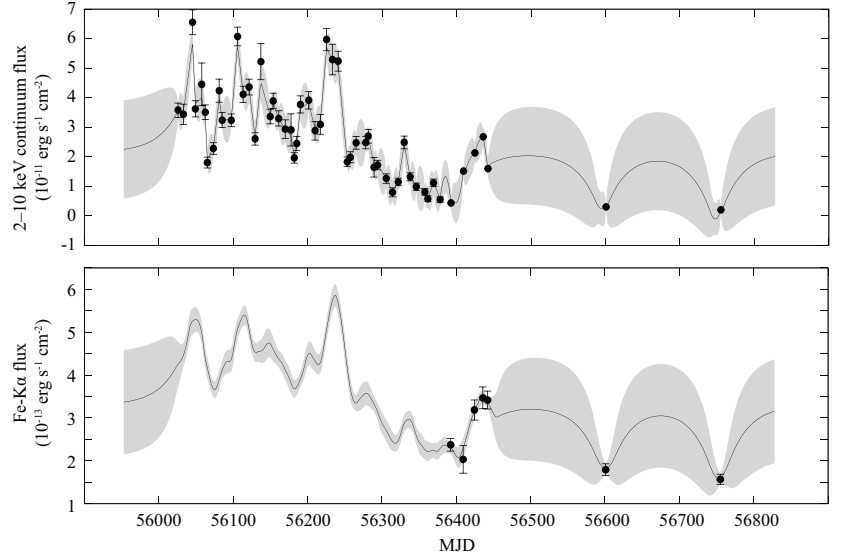
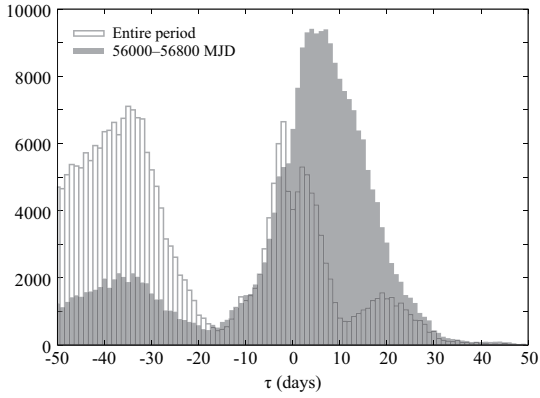


Figure 4. Results of the JAVELIN analyses, using the 2–10 keV continuum and narrow Fe-K α light-curves as the primary and response light-curves, respectively. Left panel shows the posterior distributions of the time lag τ obtained for the (open boxes) entire period and (filled boxes) MJD 56000–56800. Right panels show the best-fit light-curve models of the (top panel) 2–10 keV continuum flux and (bottom) narrow Fe-K α flux. The shaded regions correspond to 1σ uncertainties.

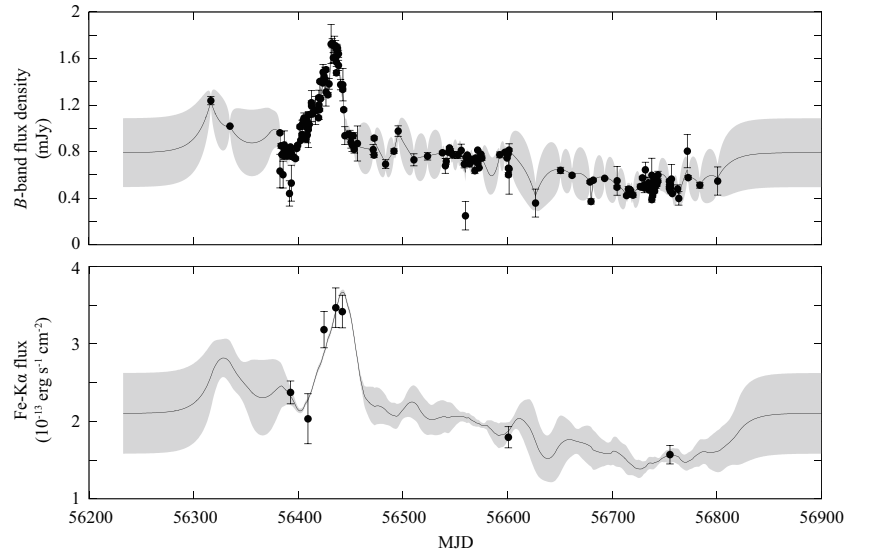
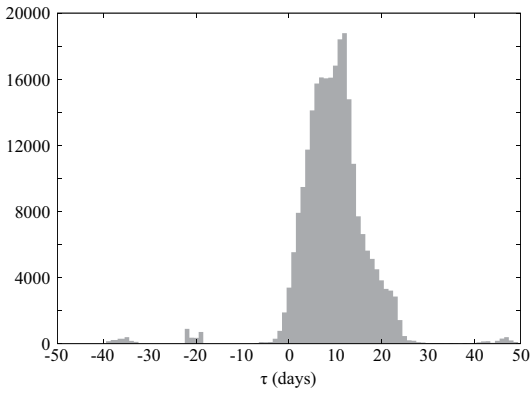


Figure 5. Same as Figure 4, but using the B -band and narrow Fe-K α light curves as the primary and response light curves, respectively.

to 56436, so this constraint is not too tight. Figure 4 (left) open-bar histogram shows the derived posterior distribution of τ . Whereas the posterior distribution showed two peaks of comparable height around $\tau \sim -30$ and 0 days, the range of $\tau \gtrsim 30$ days was ruled out at least.

Next, in order to focus on the narrow Fe-K α flare at MJD 56393–56442, which was densely covered by *Suzaku*, we limited the period to MJD 56000–56800, i.e., a period of roughly ± 400 days from the flare time. We again applied the JAVELIN analysis and showed the obtained posterior distribution of τ in the shaded histogram in Figure 4 (left). The best-fit light curves are also shown in Figure 4 (right). The median with 1σ errors was $\tau = 4.9_{-30.3}^{+10.5}$ days. The uncertainties are relatively large, in particular on the negative side,

presumably because of the sparse data after the flare peak (see the previous subsection).

So far, we had been using the 2–10 keV flux as the primary X-ray light curve. However, the Fe-K α line is actually reprocessed photons of X-rays with energies above ~ 7.1 keV. Hence, ideally, 7–10 keV light-curves should be used, the statistics permitting. We calculated the 7–10 keV fluxes from the *Suzaku* and *Swift* spectral fitting results and performed the JAVELIN analysis between the 7–10 keV continuum and narrow Fe-K α light curves at the period of MJD 56000–56800. We obtained a similar posterior distribution of the time lag of $\tau = 3.2_{-18.5}^{+9.2}$ days (the median & 1σ errors). Therefore, the 2–10 keV full range can be used for the energy range of a primary X-ray continuum to correlate with the narrow Fe-K α

Table 3. Time lags in days of the narrow Fe-K α line to the 2–10 keV continuum and B -band light curves, derived with the ICCF and JAVELIN analyses. Medians and 1σ uncertainties are tabulated.

Primary continuum	<i>Suzaku+Swift</i>	B band
ICCF (–300–300 days)	$8.0^{+12.6}_{-33.2}$	$10.9^{+4.5}_{-9.4}$
JAVELIN (–50–50 days)	$4.9^{+10.5}_{-30.3}$	$10.1^{+5.8}_{-5.6}$

line as a reasonable substitute, having better statistics and being conventional as the energy range, of the 7–10 keV band continuum.

Finally, we conducted the JAVELIN analysis using the B -band light curve as the primary continuum, which has better coverage and is reasonable (see discussion in the previous subsection and Noda et al. (2016)), instead of the 2–10 keV light curve, employing the same calculation settings. Figure 5 shows the obtained posterior distribution of τ and the best-fit light curve models. The time-lag τ was determined to be $\tau = 10.1^{+5.8}_{-5.6}$ days (the median and 1σ errors).

Both the JAVELIN analysis results of τ with the 2–10 keV continuum and B -band light-curves were found to be consistent with those obtained with the ICCF analyses. Table 3 summarizes the results.

3.4. Decoupling of the variable and stationary narrow Fe-K α components

We distinguish the variable and stationary components in the narrow Fe-K α fluxes. Since the JAVELIN algorithm ignores stationary components, we cannot directly decouple them in the ordinary routine of JAVELIN. Then, we made a correlation plot between the 2–10 keV continuum flux versus the narrow Fe-K α flux at Epochs 1–7 (Figure 6) in the following two procedures.

First, we assumed no time lag between the narrow Fe-K α flux and the 2–10 keV continuum variation. The scatter plot between them is shown in Figure 6 (black). Although it seems to have a marginally positive correlation, some large scatters remained. To test the correlation strength, we calculated the Pearson correlation coefficient. As a result, it became 0.84, with which no correlation cannot be ruled out for the number of samples of 7 with the 1% significance level. Model fitting of the plot with a linear function $y = ax + b$, where x is the 2–10 keV continuum flux and y is the Fe-K α flux, yielded an unacceptable result with $\chi^2/\text{d.o.f.} = 24.7/5$.

Next, we made the same plot, but assuming the time lag of the narrow Fe-K α flux to the 2–10 keV continuum variation of $\tau \sim 10.1$ days, which is the best-fit value derived with the JAVELIN analysis in §3.3. Because the best-fit light-curve model of the 2–10 keV continuum flux obtained by JAVELIN (Figure 4 right) includes negative values due to large uncertainties around Epoch 7, it seems unsuited to estimate interpolated fluxes. Therefore, we linearly interpolated the 2–10 keV continuum light curve obtained with *Suzaku* and *Swift* (top panel of Figure 2) and estimated the 2–10 keV continuum fluxes at the times of 10.1 days before Epochs 1–

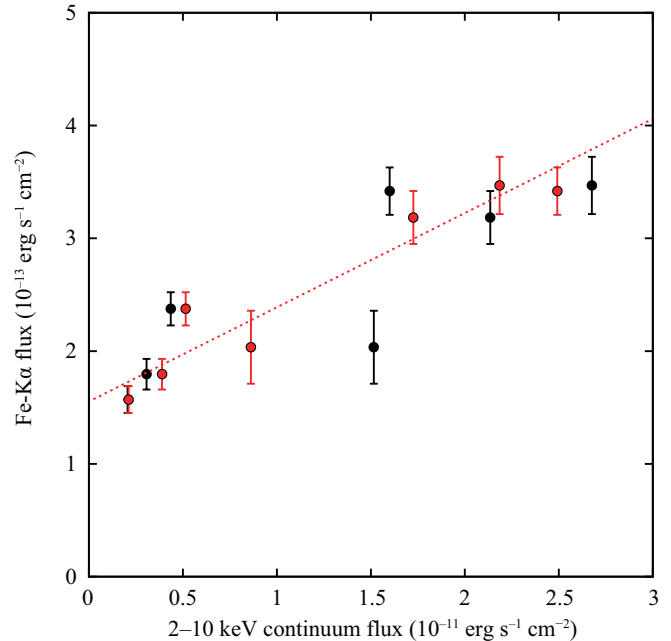


Figure 6. Correlation between the 2–10 keV continuum and narrow Fe-K α fluxes at Epochs 1–7. Black and red show the data points, in which the time lags of the Fe-K α to the 2–10 keV continuum flux are assumed to be 0 days and 10.1 days, respectively. Red dotted line shows a best-fit linear function obtained by fitting the red data points only considering the errors of narrow Fe-K α fluxes.

7, whereas the errors on the linearly-interpolated fluxes were not considered. The narrow Fe-K α fluxes and errors at Epochs 1–7 were simply the observed values at each epoch. Figure 6 (red) shows a scatter plot between the narrow Fe-K α flux and the interpolated 2–10 keV continuum variation. The Pearson correlation coefficient became 0.96 which indicates a significant positive correlation for the number of samples of 7 with the 1% significance level, showing that the positive correlation strengthened from the case with no time lag. For reference, Figure 6 (red) shows a linear function $y = ax + b$, where $a = 8.4 \times 10^{-3}$ and $b = 1.5 \times 10^{-13} \text{ erg s}^{-1} \text{ cm}^{-2}$, which are the best-fit values without considering the errors on the interpolated 2–10 keV fluxes. Around Epoch 7, in which the 2–10 keV flux got close to zero, the stationary Fe-K α flux $\sim 1.5 \times 10^{-13} \text{ erg s}^{-1} \text{ cm}^{-2}$ can be confirmed. It remained for a year (from *Suzaku* Epochs 1 to 7) regardless of the 2–10 keV continuum variability during Epochs 1–7. At Epoch 3–4, the variable Fe-K α flux which followed the X-ray continuum variation with the time lag of ~ 10.1 days got maximum, and the variable and stationary fluxes became comparable.

4. Discussion

4.1. Comparison with previous narrow Fe-K α and multi-wavelength studies

The origin of the narrow Fe-K α emission line has been discussed on many AGNs. In the past studies, one or more of the following three methods were mainly used to investigate the origin: one focusing on the variability of the line flux,

one using the line width, and the other directly imaging the spatial distribution of narrow Fe-K α lines. In this subsection, we summarize and discuss our results, comparing ours with the previous studies in the methods in the above-listed order.

4.1.1. Our results of the narrow Fe-K α line variability

The flux variability of the narrow Fe-K α line provides crucial information to constrain its emitting region, as several studies have demonstrated the point. The long-term variability on timescales of hundreds to thousands of days is common in Seyferts (e.g., Fukazawa *et al.* 2016). In the bright type-1 Seyfert NGC 4051, for example, the narrow Fe-K α flux was reported to respond possibly to the X-ray continuum flux variation of these timescales (e.g., Lamer *et al.* 2003). The short-term flux variability in days to months has been also studied in several Seyferts (e.g., Petrucci *et al.* 2002; Ponti *et al.* (2013); Marinucci *et al.* 2015; Zoghbi *et al.* 2019). Ponti *et al.* (2013) compared the short-term variation of the narrow Fe-K α flux to the X-ray continuum variation and argued that its origin was located at 40–1000 R_g from the SMBH in the bright type-1 Seyfert Mrk 509. Zoghbi *et al.* (2019) revisited the archival X-ray data of the type-1 Seyfert NGC 4151 and argued that the narrow Fe-K α variation had a time lag of ~ 3.3 days behind the X-ray continuum variation. Recently, Andonie *et al.* (2022) performed systematic studies combining the flux variability, the Full-Width Half Maximums (FWHM) (§4.1.2) and the direct imaging (§4.1.3) of the narrow Fe-K α lines and confirmed that the source sizes of the narrow Fe-K α regions are smaller than the dust sublimation radii in most AGNs. However, they did not find the short-term Fe-K α variability in NGC 4151 reported by Zoghbi *et al.* (2019). As such, the understanding of the short-term variability of AGNs is still under debate, and further studies are necessary.

In this study, we detected a significant variability of the narrow Fe-K α line in NGC 3516 on a time scale of tens of days (Figure 2). This is one of the clearest results ever obtained in any AGNs about narrow Fe-K α variations responding to the X-ray continuum. We succeeded in obtaining its time lag of $\tau \sim 10$ days behind the 2–10 keV and B -band variation with two direct methods of the ICCF and JAVELIN. The most interesting and novel point of our result is that the changing-look process occurred and NGC 3516 was in the almost type-2 (faint) phase during our 2013–2014 *Suzaku* monitoring of the source and that we successfully detected the narrow Fe-K α line variability at the faint phase.

Figure 7 shows our result in the type-2 (faint) phase, together with those of previous broad H β and dust reverberation studies while NGC 3516 was in the type-1 (bright) phase. Since the radii of the regions emitting broad H β lines depend on the luminosities, the previous results were categorized into the following two observation epochs: one in the past type-1 (bright) phase (Denney *et al.* 2010) and the other in the type-1 but relatively low-flux phase immediately after NGC 3516 started re-brightening from the type-2 (faint) phase (Feng *et al.* 2021). The dust sublimation radii obtained with near-infrared reverberation mapping with the CCF and

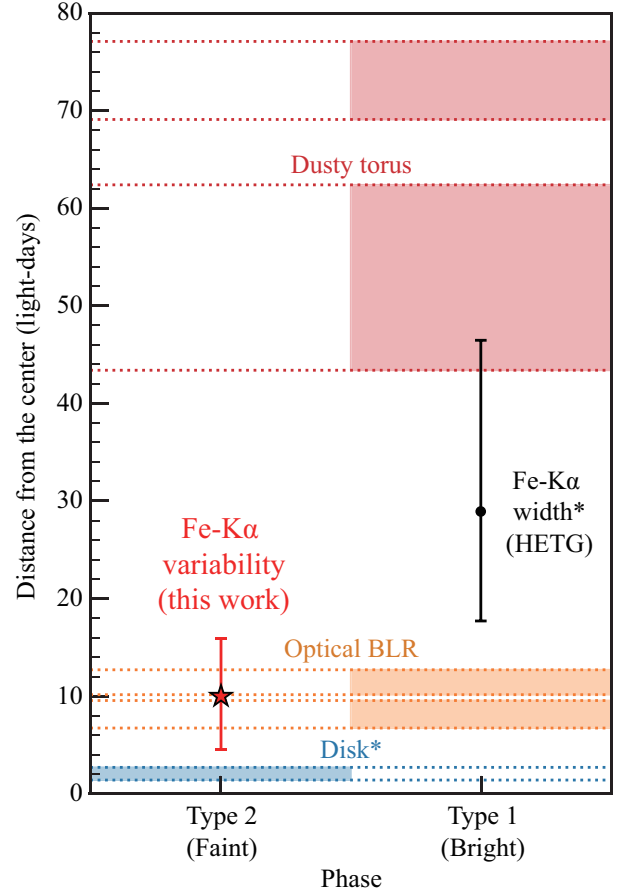


Figure 7. Comparison between the distance of the narrow Fe-K α emitting region from the center in the type-2 (faint) phase in this study (red star mark) to previous multi-wavelength studies. Blue, orange, and red shaded regions show the B -band emitting radius of the accretion disk in the type-2 phase (Noda *et al.* 2016), the distance of the BLR (Denney *et al.* 2010; Feng *et al.* 2021), and dust-reverberation radius in the type-1 phase (JAVELIN and ICCF results of Koshida *et al.* 2014 from bottom to top), respectively. The distance measured from the width of the narrow Fe-K α line in the type-1 (bright) phase (Shu *et al.* 2010) is also shown with the filled black circle. Note that the distances to the regions with asterisk marks were measured from the SMBH or an X-ray corona, whereas those without asterisk marks were measured from the optical emitting radius of ~ 2 light-days from the X-ray corona.

JAVELIN methods (Koshida *et al.* 2014) are also shown in Figure 7. The disk reverberation time lag in the type-2 (faint) phase obtained by Noda *et al.* (2016) is also shown in Figure 7. Note that although Noda *et al.* (2016) reported the B -band time lag of $2.0^{+0.7}_{-0.6}$ days (1σ errors) behind the 2–10 keV band flux, the distance from the center of the narrow Fe-K α source shown in Figure 7 does not take it into account because it is easier to compare the results of the narrow Fe-K α variation with a time lag behind the B band variation, given that the distances of the BLR and dust reverberation radius were also measured from the time lags behind the optical variation. As a result, the radius of the variable component of the narrow Fe-K α emitting region in the type-2 (faint) phase is found to be consistent with those of the broad H β line at the type-1 (bright) phase, and is significantly smaller

than the dust reverberation radii. We discuss the structure change in NGC 3516 through the changing-look process in §4.2, comparing the results in the type-1 (bright) and type-2 (faint) phases. We also discuss the origin of the stationary part of the narrow Fe-K α line in §4.1.3.

4.1.2. Previous studies of the narrow Fe-K α line width

The width of an Fe-K α line would reflect the distance of its source regions from the center of the AGN. Studies of the widths of Fe-K α lines from AGNs demand a detector with a high-energy resolution and thus have been predominantly carried out with the grating spectrometer onboard *Chandra*, the High Energy Transmission Grating (HETG), which has an energy resolution of $\Delta E/E \sim 30$ eV/6 keV at the energy of the Fe-K α line, as opposed to X-ray CCD cameras, whose energy resolution is limited to $\Delta E/E \sim 120$ eV/6 keV. In many studies, the sources of narrow Fe-K α lines are assumed to have virial motion and their energy spectra have been fitted with simple Gaussian models.

Yaqoob & Padmanabhan (2004) analyzed the HETG data of type-1 Seyferts, and reported that the weighted mean of the narrow Fe-K α core widths is ~ 2400 km s $^{-1}$. Shu et al. (2010) and Shu et al. (2011) systematically studied the line widths of the narrow Fe-K α cores of type-1 and type-2 Seyferts, respectively, by using HETG data, and reported that the mean FWHMs of their samples are ~ 2000 km s $^{-1}$ for both types. They compared the obtained widths of the Fe-K lines with those of broad H β lines and suggested that their origins are spatially distributed from regions that are a factor of ~ 2 closer to the SMBH than the BLR to those parsecs away from the SMBH, the positions differing from AGN to AGN. Minezaki & Matsushita (2015) compared the line widths of the narrow Fe-K α cores with the dust reverberation results, in addition to the widths of broad H β lines, and concluded that the Fe-K α emitting regions exist between the broad Balmer line-emitting regions and the points of the dust reverberation radii. Gandhi et al. (2015) concluded that the dust sublimation radii correspond to the outer envelopes of the narrow Fe-K α line sources in type-1 Seyferts.

The HETG data of NGC 3516 obtained circa 2000, at which NGC 3516 was in the type-1 (bright) phase, were also analyzed in the previous studies already (e.g., Turner et al. 2002; Shu et al. 2010). The velocity width of the narrow Fe-K α line was measured to be 3180_{-670}^{+880} km s $^{-1}$ (FWHM), averaging multiple observation data (Shu et al. 2010). In Figure 7, we plot the calculated corresponding radius, assuming the virial motion around the SMBH with the mass of $4.27 \times 10^7 M_{\odot}$ (Peterson et al. 2004). In the type-1 (bright) phase of NGC 3516, it cannot be ruled out that the distance from the SMBH to the region emitting the narrow Fe-K α line is same as that emitting broad H β lines, because of the large error. It is consistent with the dust reverberation radius obtained with the CCF method, whereas smaller than that obtained with the JAVELIN method reported in Minezaki & Matsushita (2015) and Gandhi et al. (2015). We note that no observations have measured the narrow Fe-K α line width of the source in the type-2 (faint) phase.

4.1.3. Comparison with previous Fe-K α imaging analyses

Direct imaging of the Fe-K α line should give the tightest constraint on the narrow Fe-K α source. The best angular resolution available in the X-ray band is $\sim 0.5''$, achieved by *Chandra*; accordingly, the finest scale that can be spatially resolved is ~ 10 pc for the nearest Seyfert galaxies or more for more distant AGNs. The first result of extended narrow Fe-K α signals was reported by Marinucci et al. (2012), and they found ~ 200 pc features in the direction of the torus in the nearby Compton-thick AGN (CTAGN), NGC 4945. Arévalo et al. (2014) imaged the narrow Fe-K α line and hard X-ray continuum in the CTAGN, Circinus Galaxy, and found that they are extended in the direction of the bicone up to several hundreds pc. Kawamuro et al. (2019) also reported that some narrow Fe-K α flux is produced at molecular clouds located ~ 60 pc away from the center in Circinus Galaxy, and argued that the fraction of the extended narrow Fe-K α is $\sim 10\%$, while the rest ($\sim 90\%$) is produced in a central region within ~ 10 pc. Bauer et al. (2015) studied the spatial distribution of the narrow Fe-K α line in the nearby CTAGN, NGC 1068, and found that 30% of the line arises from the region broader than ~ 140 pc from the center. Nakata et al. (2021) also reported that the narrow Fe-K α flux is produced at molecular clouds located several tens of parsecs away from the center in NGC 1068. Fabbiano et al. (2017) discovered the narrow Fe-K α signals extended to a kpc scale in the CTAGN, ESO 428-G014. Like these, extended narrow Fe-K α emissions have been found in multiple CTAGNs, while there are no report on type-1 (and changing-look) sources so far.

In §3.4, we decoupled the variable and stationary components of the narrow Fe-K α flux of NGC 3516, and it is possible that the stationary component corresponds to the extended narrow Fe-K α line beyond a torus scale of a few tens pc. To check the contribution of the extended emission, we merged and analyzed the *Chandra*/HETG data of NGC 3516 (ObsID: 2080, 2431, 2482, 7281, 7282, 8450, 8451, 8452). Although the HETG data were obtained during the type-1 phase, it can be used to estimate the extended flux. First, we made a radial distribution of 6–7 keV counts per pixel from the 0th order data, and compared it with the point spread function (PSF) created by Kawamuro et al. (2021). As a result, the radial distribution did not show significant excess counts from the PSF. Next, we made an image from the 0th order data, and extracted a 2–7 keV spectrum from the 2–4'' annular region which corresponds to ~ 400 –800 pc from the center. Here, we set the inner radius to be 2'', because a region within 2'' is affected by strong pile-up effects. Considering the flux leakage from the point source at the nucleus, we fitted the 2–7 keV spectrum, and estimated the Fe-K α flux to be $4.9_{-3.3}^{+3.5} \times 10^{-15}$ erg s $^{-1}$ cm $^{-2}$ (1σ errors) which is ~ 30 times smaller than the stationary component. Hence, the stationary component is considered to mainly come from a region within ~ 400 pc. Our observations suggest that the stationary component remained stable for ~ 1 year (Epochs 1–7). Then, the lower limit of the size of its emitting region is estimated to be ~ 0.3 pc. We thus conclude that a large part

of the stationary component is likely to be produced at regions located from ~ 0.3 to ~ 400 pc away from the SMBH, which includes the locations of the dusty torus and the extended molecular region.

4.2. Structure change and the origin of the BLR

4.2.1. Structure of the BLR at the type-2 phase

The disappearance of the broad emission lines at a (changing-look) transition of the AGN type from type 1 to 2 means some drastic change in the state of the BLR, along with a drastic drop in the mass-accretion rate. Two major scenarios for the BLR state change are physical disappearance of the BLR materials and the deactivation of the emission-line production mechanism (see Introduction).

In this study, we revealed that the radius of the narrow Fe-K α emitting region is ~ 10 light-days in the type-2 (faint) phase (Figure 7). The radius is consistent with that of the broad H β emitting region in the type-1 (bright) phase. This result therefore supports the second scenario, i.e., the emission-line production was deactivated in the type-2 phase while the BLR materials remained at the same locations as in the type-1 phase. The equivalent width (EW) of the narrow Fe-K α line is another independent parameter useful to validate the hypothesis because the EW is a function of the product of the covering factor and the column density of the narrow Fe-K α source. Given that EWs are known to depend on X-ray brightness, we should only compare EWs at epochs with similar 2–10 keV fluxes (F_{2-10}). According to Shu *et al.* (2010), NGC 3516 in a type-1 phase showed $\text{EW} = 83^{+28}_{-26}$ eV at $F_{2-10} = 2.3 \times 10^{-11}$ erg s $^{-1}$ cm $^{-2}$ (HETG ObsID:2482). By contrast, the source in a type-2 phase in this study showed $\text{EW} = 122 \pm 9$ eV at $F_{2-10} = 2.7 \times 10^{-11}$ erg s $^{-1}$ cm $^{-2}$ (Epoch 4 where the source showed the smallest EW and the highest 2–10 keV flux during the *Suzaku* monitoring; Table 2). This fact likely suggests that neither the covering factor nor the column density of the materials emitting the narrow Fe-K α line considerably changed between the type-1 and -2 phases.

Another important question is whether the BLR materials in the type-2 phase, which cannot be detected in optical observations, are in the dust-free gas or dust phases. If their degree of ionization/excitation simply decreases following the rapid UV continuum drops in the changing-look process, they should remain in the dust-free gas phase. However, Kokubo & Minezaki (2020) suggested that in a CLAGN Mrk 590, the inner radius of the dust distribution in the type-2 phase decreased to the radius of the BLR in the type-1 phase in less than 4 years after a changing-look process. They interpreted the result in conjunction with potential new dust formation at the distance of the BLR from the SMBH on short timescales of years. If short-term dust formation commonly occurs in the turning-off changing-look process, the BLR materials in the type-2 phase of NGC 3516 might be also in the dust phase.

The most decisive observational method to distinguish the dust-free gas and dust phases is to monitor the variability of

the near-infrared flux, which originates at the dust sublimation radius (dust reverberation mapping; e.g., Koshida *et al.* 2014; Minezaki *et al.* 2019; Noda *et al.* 2020), simultaneously with monitoring of the X-ray continuum, optical, and narrow Fe-K α emission fluxes. Then, if the narrow Fe-K α time lag is shorter than the dust reverberation time lag, the BLR materials must be in the dust-free gas, and if longer, in the dust phase.

4.2.2. Constraints to the origin of the BLR

Can the origin of the BLR be constrained with our results of the narrow Fe-K α reverberation mapping? The following four scenarios are the major ones that have been proposed to explain the origin of the BLR, as summarized by Czerny (2019): (1) an inflow in which BLR materials come from outer regions, such as dusty tori (e.g., Hu *et al.* 2008; Ferland *et al.* 2009), (2) in-situ formation through accretion disk fragmentation and star formation (e.g., Collin & Zahn 1999; Collin & Zahn 2008; Wang *et al.* 2011), (3) the static disk atmosphere puffed up by the dust radiation pressure from the accretion disk (e.g., Baskin & Laor 2018), (4) accretion disk wind which is driven by radiation pressure via lines (e.g., Murray & Chiang 1995) or dusts (e.g., Czerny & Hryniewicz 2011). Because of the presence of winds from accretion disks in many AGNs (e.g., Tombesi *et al.* 2013), the last two scenarios are attracting attentions, and hotly debated recently.

In scenarios (1) and (2), the location of the BLR materials are not directly affected by the luminosity variation in the central engine. Hence, it is difficult to test them by the present results. By contrast, in scenarios (3) and (4), the location of the BLR materials is determined according to the balance between the SMBH gravity and the radiative pressure from the accretion disk; then, the location must be affected by the luminosity drop during the changing-look process. According to Baskin & Laor (2018) on the third scenario, the peak-height radius of the puffed-up disk, R_{max} , which represents the BLR location, has a relatively high luminosity dependence of $R_{\text{max}} \propto L^{0.59}$, and accordingly, the BLR radius should decrease by a factor of ~ 4 when the luminosity decreases by a factor of 10. Therefore, their prediction is inconsistent with our result that the BLR materials during the type-2 (faint) phase remained at almost the same distance as in the type-1 (bright) phase. However, given that the type-2 phase during which we performed the *Suzaku* monitoring was only ~ 1 year after the luminosity decrease due to the changing-look process started in NGC 3516 at MJD 56000 (Ilić *et al.* 2020), it is possible that one-year duration was too short for the geometry of the BLR to change significantly; it should be on the dynamical timescale. To furthermore test scenario (3) and (4), it is crucial to perform narrow Fe-K α reverberation mapping on CLAGNs after both their type-changes and transition of the geometry of the BLR are completed.

As reported in Mehdipour *et al.* (2022), NGC 3516 was observed by *Chandra*/Low Energy Transmission Grating (LETG), *NuSTAR*, and *Swift* almost simultaneously in 2017 during which it was still in the faint phase. These are the data obtained ~ 5 years after the changing-look process

started, and the change of the BLR geometry is considered to have more proceeded. Because *Chandra*/LETG does not cover a range above 3 keV, we focused the *NuSTAR* and *Swift* data. We reduced the *NuSTAR* data (ObsID: 603020160[02, 04, 06, 08, 10, 12]) with similar manners to those in Mehdipour et al. (2022), and obtained the 2–10 keV continuum fluxes ($\sim (0.5 - 1.4) \times 10^{-11} \text{ erg s}^{-1} \text{ cm}^{-2}$) and the narrow Fe-K α fluxes ($\sim 2.1 \times 10^{-13} \text{ erg s}^{-1} \text{ cm}^{-2}$) in 2017 Dec by spectral fits with the same model as those in the *Suzaku* spectral fits in §3.1. We also analyzed the *Swift* data in MJD 57960.4–58117.5 (2017 Jul–Dec), and obtained the 2–10 keV continuum fluxes from the individual observations by the same manners as in §3.1. As a result, the significant variability of the narrow Fe-K α flux was not detected among the *NuSTAR* observations, and hence, we cannot constrain the time lag of the narrow Fe-K α flux behind the 2–10 keV flux in 2017 by applying the ICCF or JAVELIN analyses. Therefore, it is essential to detect significant variability of the narrow Fe-K α line for further tests of the formation models of the BLR in future monitors.

4.2.3. Future observations with X-ray microcalorimeters

The narrow Fe-K α reverberation mapping can be conducted with currently operational X-ray CCD and/or grating detectors in orbit, as we have demonstrated in this study. However, observations with X-ray microcalorimeters, which have unprecedentedly high energy resolution of $\Delta E/E \lesssim 7 \text{ eV}/6 \text{ keV}$, are expected to bring a technical leap in narrow Fe-K α reverberation mapping. Hitomi Collaboration (2018) performed ultra-high-quality spectroscopy on the narrow Fe-K α line emission from the AGN NGC 1275 with the X-ray microcalorimeter onboard *Hitomi*, which was the first X-ray microcalorimeter observation of an AGN. They detected a very weak (EW $\sim 20 \text{ eV}$) and narrow (velocity width of 900–1600 km s $^{-1}$) Fe-K α line, which could be detected with neither X-ray CCD cameras nor grating detectors. As such, X-ray microcalorimeters will enable us to detect even modest (or weak) variability of narrow Fe-K α lines. The X-Ray Imaging Spectrometer Mission (*XRISM*) with the X-ray microcalorimeter Resolve is scheduled to be launched in 2023, and the launch of the Advanced Telescope for High ENergy Astrophysics (*Athena*) with the X-ray microcalorimeter X-IFU is planned in the 2030s. Narrow Fe-K α reverberation mapping with the X-ray microcalorimeters onboard *XRISM* and *Athena* will reveal the structures of AGNs and their origins in great detail and precision.

5. Conclusions

With the *Suzaku*, *Swift* and optical simultaneous monitoring observations of the CLAGN NGC 3516 in the almost type-2 (faint) phase, we detected the flux variability of the narrow Fe-K α emission line at 6.4 keV on a timescale of tens of days, which is correlated with the 2–10 keV and *B*-band continuum variations. We performed the narrow Fe-K α reverberation mapping with the 2–10 keV continuum, *B* band, and narrow Fe-K α line light-curves, and succeeded in determining the narrow Fe-K α time lag to be $10.1_{-5.6}^{+5.8}$ days

behind the continuum. The narrow Fe-K α emitting radius in the type-2 (faint) phase is consistent with that of the BLR materials in the type-1 (bright) phase. This implies that even while the CLAGN was in the type-2 phase during the changing-look process, the BLR materials remained at the same location as in the type-1 phase and were deactivated from producing optical broad lines through the rapid drop of the ionizing/exciting UV flux, which is presumably caused by the state transition of the accretion flow onto the SMBH. The result might be inconsistent with the hotly-discussed formation models of the BLR which propose that the radiative pressure from the accretion disk should be the main driving force, given that the radiation would become too weak to sustain the BLR materials at the same location during the type-2 phase if our interpretation of our result is the case. This study demonstrates the efficiency of the narrow Fe-K α reverberation mapping for revealing the structure of AGNs and its formation mechanism. The method is applicable in a far more effective way to data obtained with the X-ray microcalorimeters onboard the scheduled astronomical X-ray satellites *XRISM* and *Athena*.

We thank the anonymous referee for his/her valuable suggestions and comments. This study is supported by Japan Society for the Promotion of Science (JSPS) KAKENHI with Grant numbers of 19K21884 (HN), 20H00175 (HM), 20H00178 (HM), 20H01941 (HN), 20H01947 (HN), 20K14529 (TK), 22K03683 (HS) and 22K20391(SY). SY is grateful for support from RIKEN Special Postdoctoral Researcher Program. This work made use of data supplied by the UK Swift Science Data Centre at the University of Leicester.

References

- Andonie C., Bauer F. E., Carraro R., Arévalo P., Alexander D. M., Brandt W. N., Buchner J., et al., 2022, *A&A*, 664, A46. doi:10.1051/0004-6361/202142473
- Antonucci R. R. J., Miller J. S., 1985, *ApJ*, 297, 621. doi:10.1086/163559
- Antonucci R., 1993, *ARA&A*, 31, 473. doi:10.1146/annurev.aa.31.090193.002353
- Arévalo P., Bauer F. E., Puccetti S., Walton D. J., Koss M., Boggs S. E., Brandt W. N., et al., 2014, *ApJ*, 791, 81. doi:10.1088/0004-637X/791/2/81
- Baskin A., Laor A., 2018, *MNRAS*, 474, 1970. doi:10.1093/mnras/stx2850
- Bauer F. E., Arévalo P., Walton D. J., Koss M. J., Puccetti S., Gandhi P., Stern D., et al., 2015, *ApJ*, 812, 116. doi:10.1088/0004-637X/812/2/116
- Collin S., Zahn J.-P., 1999, *A&A*, 344, 433
- Collin S., Zahn J.-P., 2008, *A&A*, 477, 419. doi:10.1051/0004-6361:20078191
- Czerny B., Hryniewicz K., 2011, *A&A*, 525, L8. doi:10.1051/0004-6361/201016025
- Czerny B., 2019, *OAst*, 28, 200. doi:10.1515/astro-2019-0018
- Denney K. D., Peterson B. M., Pogge R. W., Adair A., Atlee D. W., Au-Yong K., Bentz M. C., et al., 2010, *ApJ*, 721, 715. doi:10.1088/0004-637X/721/1/715
- Dewangan G. C., Griffiths R. E., Di Matteo T., Schurch N. J., 2004, *ApJ*, 607, 788. doi:10.1086/383607

- Evans P. A., Beardmore A. P., Page K. L., Tyler L. G., Osborne J. P., Goad M. R., O'Brien P. T., et al., 2007, *A&A*, 469, 379.
doi:10.1051/0004-6361:20077530
- Evans P. A., Beardmore A. P., Page K. L., Osborne J. P., O'Brien P. T., Willingale R., Starling R. L. C., et al., 2009, *MNRAS*, 397, 1177.
doi:10.1111/j.1365-2966.2009.14913.x
- Fabbiano G., Elvis M., Paggi A., Karovska M., Maksym W. P., Raymond J., Risaliti G., et al., 2017, *ApJL*, 842, L4. doi:10.3847/2041-8213/aa7551
- Ferland G. J., Hu C., Wang J.-M., Baldwin J. A., Porter R. L., van Hoof P. A. M., Williams R. J. R., 2009, *ApJL*, 707, L82.
doi:10.1088/0004-637X/707/1/L82
- Feng H.-C., Hu C., Li S.-S., Liu H. T., Bai J. M., Xing L.-F., Wang W.-Y., et al., 2021, *ApJ*, 909, 18. doi:10.3847/1538-4357/abd851
- Fukazawa Y., Furui S., Hayashi K., Ohno M., Hiragi K., Noda H., 2016, *ApJ*, 821, 15. doi:10.3847/0004-637X/821/1/15
- Gandhi P., Hönig S. F., Kishimoto M., 2015, *ApJ*, 812, 113.
doi:10.1088/0004-637X/812/2/113
- Graham M. J., Ross N. P., Stern D., Drake A. J., McKernan B., Ford K. E. S., Djorgovski S. G., et al., 2020, *MNRAS*, 491, 4925.
doi:10.1093/mnras/stz3244
- Hitomi Collaboration, Aharonian F., Akamatsu H., Akimoto F., Allen S. W., Angelini L., Audard M., et al., 2018, *PASJ*, 70, 13.
doi:10.1093/pasj/psx147
- Hu C., Wang J.-M., Ho L. C., Chen Y.-M., Zhang H.-T., Bian W.-H., Xue S.-J., 2008, *ApJ*, 687, 78. doi:10.1086/591838
- Ilić D., Oknyansky V., Popović L. Č., Tsygankov S. S., Belinski A. A., Tatarnikov A. M., Dodin A. V., et al., 2020, *A&A*, 638, A13.
doi:10.1051/0004-6361/202037532
- Ishisaki Y., Maeda Y., Fujimoto R., Ozaki M., Ebisawa K., Takahashi T., Ueda Y., et al., 2007, *PASJ*, 59, 113. doi:10.1093/pasj/59.sp1.S113
- Kawamuro T., Izumi T., Imanishi M., 2019, *PASJ*, 71, 68.
doi:10.1093/pasj/psz045
- Kawamuro T., Ricci C., Izumi T., Imanishi M., Baba S., Nguyen D. D., Onishi K., 2021, *ApJS*, 257, 64. doi:10.3847/1538-4365/ac2891
- Khachikian E. Y., Weedman D. W., 1974, *ApJ*, 192, 581.
doi:10.1086/153093
- Kokubo M., Minezaki T., 2020, *MNRAS*, 491, 4615.
doi:10.1093/mnras/stz3397
- Koshida S., Minezaki T., Yoshii Y., Kobayashi Y., Sakata Y., Sugawara S., Enya K., et al., 2014, *ApJ*, 788, 159. doi:10.1088/0004-637X/788/2/159
- Koyama K., Tsunemi H., Dotani T., Bautz M. W., Hayashida K., Tsuru T. G., Matsumoto H., et al., 2007, *PASJ*, 59, 23.
doi:10.1093/pasj/59.sp1.S23
- LaMassa S. M., Cales S., Moran E. C., Myers A. D., Richards G. T., Eracleous M., Heckman T. M., et al., 2015, *ApJ*, 800, 144.
doi:10.1088/0004-637X/800/2/144
- Lamer G., McHardy I. M., Uttley P., Jahoda K., 2003, *MNRAS*, 338, 323.
doi:10.1046/j.1365-8711.2003.06005.x
- MacLeod C. L., Ross N. P., Lawrence A., Goad M., Horne K., Burgett W., Chambers K. C., et al., 2016, *MNRAS*, 457, 389.
doi:10.1093/mnras/stv2997
- Makishima K., Maejima Y., Mitsuda K., Bradt H. V., Remillard R. A., Tuohy I. R., Hoshi R., et al., 1986, *ApJ*, 308, 635. doi:10.1086/164534
- Marinucci A., Risaliti G., Wang J., Nardini E., Elvis M., Fabbiano G., Bianchi S., et al., 2012, *MNRAS*, 423, L6.
doi:10.1111/j.1745-3933.2012.01232.x
- Marinucci A., Matt G., Bianchi S., Lu T. N., Arevalo P., Baloković M., Ballantyne D., et al., 2015, *MNRAS*, 447, 160.
doi:10.1093/mnras/stu2439
- Matt G., Guainazzi M., Maiolino R., 2003, *MNRAS*, 342, 422.
doi:10.1046/j.1365-8711.2003.06539.x
- Mehdipour M., Kriss G. A., Brenneman L. W., Costantini E., Kaastra J. S., Branduardi-Raymont G., Di Gesu L., et al., 2022, *ApJ*, 925, 84.
doi:10.3847/1538-4357/ac42ca
- Merloni A., Dwelly T., Salvato M., Georgakakis A., Greiner J., Krumpe M., Nandra K., et al., 2015, *MNRAS*, 452, 69. doi:10.1093/mnras/stv1095
- Miller J. S., Goodrich R. W., 1990, *ApJ*, 355, 456. doi:10.1086/168780
- Minezaki T., Matsushita K., 2015, *ApJ*, 802, 98.
doi:10.1088/0004-637X/802/2/98
- Minezaki T., Yoshii Y., Kobayashi Y., Sugawara S., Sakata Y., Enya K., Koshida S., et al., 2019, *ApJ*, 886, 150. doi:10.3847/1538-4357/ab4f7b
- Mitsuda K., Inoue H., Koyama K., Makishima K., Matsuoka M., Ogawara Y., Shibazaki N., et al., 1984, *PASJ*, 36, 741
- Murray N., Chiang J., 1995, *ApJL*, 454, L105. doi:10.1086/309775
- Nakata R., Hayashida K., Noda H., Yoneyama T., Matsumoto H., Imanishi M., 2021, *PASJ*, 73, 338. doi:10.1093/pasj/psab001
- Nandra K., O'Neill P. M., George I. M., Reeves J. N., 2007, *MNRAS*, 382, 194. doi:10.1111/j.1365-2966.2007.12331.x
- Noda H., Makishima K., Yamada S., et al. 2011, *PASJ*, 63, S925
- Noda H., Makishima K., Nakazawa K., et al. 2013b, *PASJ*, 65, 4
- Noda H., Minezaki T., Watanabe M., et al. 2016, *ApJ*, 828, 78
- Noda H., Minezaki T., Watanabe M., Kokubo M., Kawaguchi K., Itoh R., Morihana K., et al., 2016, *yCat*, JApJ/828/78
- Noda H., Done C., 2018, *MNRAS*, 480, 3898
- Noda H., Kawamuro T., Kokubo M., Minezaki T., 2020, *MNRAS*, 495, 2921. doi:10.1093/mnras/staa1376
- Osterbrock D. E., 1977, *ApJ*, 215, 733. doi:10.1086/155407
- Osterbrock D. E., 1981, *ApJ*, 249, 462. doi:10.1086/159306
- Oknyansky V. L., Brotherton M. S., Tsygankov S. S., Dodin A. V., Bao D.-W., Zhao B.-X., Du P., et al., 2021, *MNRAS*, 505, 1029.
doi:10.1093/mnras/stab1138
- Peterson B. M., Wanders I., Horne K., Collier S., Alexander T., Kaspi S., Maoz D., 1998, *PASP*, 110, 660. doi:10.1086/316177
- Peterson B. M., Ferrarese L., Gilbert K. M., Kaspi S., Malkan M. A., Maoz D., Merritt D., et al., 2004, *ApJ*, 613, 682. doi:10.1086/423269
- Petrucchi P. O., Henri G., Maraschi L., Ferrando P., Matt G., Mouchet M., Perola C., et al., 2002, *A&A*, 388, L5. doi:10.1051/0004-6361:20020534
- Ponti G., Cappi M., Costantini E., Bianchi S., Kaastra J. S., De Marco B., Fender R. P., et al., 2013, *A&A*, 549, A72.
doi:10.1051/0004-6361/201219450
- Ricci C., Paltani S., Ueda Y., Awaki H., 2013, *MNRAS*, 435, 1840.
doi:10.1093/mnras/stt1326
- Ruan J. J., Anderson S. F., Cales S. L., Eracleous M., Green P. J., Morganson E., Runnoe J. C., et al., 2016, *ApJ*, 826, 188.
doi:10.3847/0004-637X/826/2/188
- Ruan J. J., Anderson S. F., Eracleous M., Green P. J., Haggard D., MacLeod C. L., Runnoe J. C., et al., 2019, *ApJ*, 883, 76.
doi:10.3847/1538-4357/ab3c1a
- Seyfert C. K., 1943, *ApJ*, 97, 28. doi:10.1086/144488
- Shakura, N. I., & Sunyaev, R. A. 1973, *A&A*, 24, 337
- Shapovalova A. I., Popović, L. Č., Afanasiev V. L., Ilić, D., Kovačević, et al., 2019, *MNRAS*, 485, 4790. doi:10.1093/mnras/stz692
- Shu X. W., Yaqoob T., Wang J. X., 2010, *ApJS*, 187, 581.
doi:10.1088/0067-0049/187/2/581
- Shu X. W., Yaqoob T., Wang J. X., 2011, *ApJ*, 738, 147.
doi:10.1088/0004-637X/738/2/147
- Takahashi T., Abe K., Endo M., Endo Y., Ezoe Y., Fukazawa Y., Hamaya M., et al., 2007, *PASJ*, 59, 35. doi:10.1093/pasj/59.sp1.S35
- Tombesi F., Cappi M., Reeves J. N., Nemmen R. S., Baito V., Gaspari M., Reynolds C. S., 2013, *MNRAS*, 430, 1102. doi:10.1093/mnras/sts692
- Turner T. J., Mushotzky R. F., Yaqoob T., George I. M., Snowden S. L., Netzer H., Kraemer S. B., et al., 2002, *ApJL*, 574, L123.
doi:10.1086/342504
- Urry C. M., Padovani P., 1995, *PASP*, 107, 803. doi:10.1086/133630
- Wang J.-M., Ge J.-Q., Hu C., Baldwin J. A., Li Y.-R., Ferland G. J., Xiang F., et al., 2011, *ApJ*, 739, 3. doi:10.1088/0004-637X/739/1/3
- Yaqoob T., Padmanabhan U., 2004, *ApJ*, 604, 63. doi:10.1086/381731
- Yuan F., Narayan R., 2014, *ARA&A*, 52, 529.
doi:10.1146/annurev-astro-082812-141003

Zoghbi A., Miller J. M., Cackett E., 2019, ApJ, 884, 26.

doi:10.3847/1538-4357/ab3e31

Zu Y., Kochanek C. S., Peterson B. M., 2011, ApJ, 735, 80.

doi:10.1088/0004-637X/735/2/80

Zu Y., Kochanek C. S., Kozłowski S., Udalski A., 2013, ApJ, 765, 106.

doi:10.1088/0004-637X/765/2/106